Original Article

Quantitative Assessment of Photoneutron-induced Secondary Radiation Dose in Prostate Treatment Using an 18 MV Medical Linear Accelerator: A Monte Carlo Study

Mustapha Assalmi, Abdullah Alshreef[1,2], EL Yamani Diaf[3], Assia Arectout[4], Nicholas Ade[5,6], El Hassan El Berhdadi[7]

National Center for Energy and Nuclear Science and Technology (CNESTEN), Rabat, [3]Laboratory of Biology, Geoscience, Physics and Environment (LBGPE), Multidisciplinary Faculty of Nador, Mohammed First University, Oujda, [4]Laboratory of Radiations and Nuclear Systems, Faculty of Sciences, University Abdelmalek Essaadi, Tetouan, [7]Engineering Sciences and Applications Laboratory National School of Applied Sciences Al-Hoceima, Morocco, [1]Department of Radiation Oncology, University of Minnesota, Minneapolis, MN, USA, [2]Depatment of Biomedical Physics, King Faisal Specialist Hospital and Research Centre, Riyadh, Saudi Arabia, [5]Department of Physics, The University of Bamenda, P.O Box 39, Bambili, [6]Cameroon Oncology Center, Douala, Cameroon

Abstract

Purpose: This study aims to quantify the secondary radiation dose caused by photoneutrons during prostate cancer treatment using an 18 MV medical linear accelerator (LINAC) through Monte Carlo simulations and experimental validation. **Methods:** Monte Carlo simulations were performed using G4Linac_MT to model the 18 MV photon beam of an Elekta LINAC. The simulation results were validated against experimental measurements. Neutron characteristics, including penetration, cross-section interactions, Linear Energy Transfer (LET), and dose contributions, were analyzed using an adult male ICRP phantom. Prostate treatment scenarios involved 3D-CRT plans with 4-fields, 5-fields, and 7-fields. Specific absorbed fractions (SAFs) in various organs were also evaluated. **Results:** Simulation and experimental measurements showed strong agreement, with a dose error of approximately 0.74%, and 97% of dose points passed a 2%/2 mm gamma index. Intermediate neutrons constituted 87.05%, while 12.95% were fast neutrons. Neutron dose contributions were 0.63%, 0.33%, and 0.77% for the 3D-CRT 4-field, 5-field, and 7-field plans, respectively. SAF values decreased as neutron energy increased, highlighting reduced neutron interaction efficiency at higher energies. **Conclusions:** Monte Carlo simulation is a reliable approach for evaluating neutron dose contributions in high-energy X-ray LINACs. Optimization of treatment plans is essential to minimize neutron-induced dose contributions.

Keywords: Absorbed fractions, medical linear accelerator, Monte Carlo simulation, neutron energy, photoneutrons, prostate treatment, secondary radiation dose

Received on: 12-08-2024 **Review completed on: 26-10-2024** **Accepted on: 12-11-2024** **Published on: 18-12-2024**

Introduction

Radiation therapy is an essential and commonly used treatment modality for solid cancers.[1-3] However, the effectiveness of this treatment relies on the minimization of radiation side effects on healthy organs.[3,4] This remains a major challenge in current developments, with experiments being conducted on flash very high-energy electron and proton modes.[5-8] An inherent challenge within conventional high-energy photon-mode radiotherapy, which is typically used to treat deep-seated tumors, is that it is accompanied by contamination particles, notably neutrons, which are not planned in the treatment planning system (TPS).[9,10] Neutrons, particles with a mass of around 1.6749×10^{-27} kg and no electrical charge, are created in LINAC head by a process known as photonuclear absorption. This process takes place when photons with energies in excess of 8 MeV interact with atomic nuclei. One or more neutrons are then produced as a result of this interaction. Neutron particles exhibit an elevated linear energy transfer (LET), a characteristic that amplifies their potential to induce adverse side effects within the patient's body.[11-14] Furthermore, other particles, such as electrons and positrons, also appear with

Access this article online

Quick Response Code:

Website: www.jmp.org.in

DOI: 10.4103/jmp.jmp_141_24

Address for correspondence: Dr. Mustapha Assalmi, National Center for Energy Sciences and Nuclear Techniques, B.P. 1382 R.P. 10001, Rabat, Morocco.
E-mail: m.assalmi@ump.ac.ma

How to cite this article: Assalmi M, Alshreef A, Diaf EL Y, Arectout A, Ade N, Barhdadi El H. Quantitative assessment of photoneutron-induced secondary radiation dose in prostate treatment using an 18 MV medical linear accelerator: A Monte Carlo study. J Med Phys 2024;49:673-86.

high photon energies under indirect ionization and excitation of the matter crossed. TPSs integrate the contribution of these particles into the overall dose calculation, focusing on their concentration near the skin surface.

Recent studies have explored neutron production in high-energy photon LINACs, highlighting the potential impact of secondary neutron doses in radiotherapy environments. Tai *et al*.[15] measured neutron dose equivalents in LINAC treatment vaults, indicating significant neutron dose distributions in clinical environments, particularly near LINAC components that generate photoneutrons during high-energy photon therapy. Similarly, Dowlatabadi *et al*.[16] examined photoneutron production in Siemens LINACs using Monte Carlo simulations, demonstrating variations in neutron production based on field size and specific LINAC components. Assalmi and Diaf[11] further explored neutron production relative to LINAC field configurations and compared the depth dose deposition of neutrons with other secondary particles generated by an 18 MV photon beam. This study demonstrated the high penetration capacity of neutrons and their wide spatial distribution, particularly in small fields where the collimators are in the path of high-energy photon beams. This alignment increases the probability of neutron production by photon disintegration, underlining the significant impact of LINAC fields on neutron contamination levels.

In the present study, we compared neutron dose contributions in different three-dimensional conformal radiotherapy (3D-CRT) treatment plans. The study highlights differences in neutron exposure depending on the radiotherapy technique used, aiming to optimize treatment planning and reduce unintended neutron doses. Specifically, we quantified neutron contributions in prostate cancer treatment across three distinct plans: 3D-CRT with 4 fields, 3D-CRT with 5 fields, and 3D-CRT with 7 fields. This analysis illustrates the relationship between neutron contribution and high-energy photon beams in treatment fields. Providing insights to enhance treatment strategies and optimize dose delivery, ultimately improving clinical practice. In addition, we analyzed scenarios where neutrons with quantified energy levels (0.005 MeV to 3 MeV) reach the organs around the prostate.

To further the aims of this study, we investigate the dose deposition characteristics of neutron beams from the 18 MV source in elements commonly found in human soft tissue, including hydrogen (H, 10.5%), carbon (C, 22.6%), oxygen, and nitrogen (N, 2.34%).[17] In addition, our research highlights the ability of detected neutrons to penetrate and deposit doses in high-density media. We are exploring the comparison of the dose fraction between the total dose delivered by the 18 MV beam and the neutron contribution in a water phantom. In addition, our work involves investigating the neutron dose contribution in prostate treatments, using a voxelized ICRP110 human-adult phantom.[18] This study also includes the calculation of the specific absorption fraction (SAF) of neutrons detected in the various organs. To achieve these objectives, a Monte Carlo simulation was run using an Elekta medical accelerator configured for an 18 MV photon beam. The geometric accuracy of the Elekta LINAC was validated by measurements of the depth dose distribution (PDD) and lateral dose distribution (profiles) in a water phantom, including different irradiation field sizes. To understand the nature of the neutrons created at 18 MV, we are tracking their appearance in the geometric construction of LINAC. This involves determining the role of the individual LINAC components in the photonuclear reaction, and classifying the detected neutrons into two distinct groups: 87.05% intermediate neutrons ($0.0003 \leq E < 1$ MeV) and 12.95% fast neutrons ($E \geq 1$ MeV). Our study also includes a quantitative analysis of the kinetic energy of the neutrons detected. This evaluation also includes characterizing the spatial dispersion of these neutrons across the radial and angular dimensions of phase space.

Materials and Methods

Monte Carlo modeling

The simulation and quantification of neutron particles generated from 18MV photons were performed using the G4 Linac_MT version 2, developed by El Bakkali *et al*.[19] In this study, the high performance of the HPC-Marwan computing grid[20] was used to carry out simulations with reduced statistical uncertainties and a significant gain in computing time.[21] The flexibility of this code enables us to detect the characteristics of secondary particles, including their type, kinetic energy, and point of origin. Using this statistical data, we can calculate the dose deposited by each particle type. By using the Particle Data Group (PDG) identifier to characterize each particle type stored in phase space, we can then use it as a radiation source for dose calculations.

In the present investigation, the geometry of the Elekta Synergy linear medical accelerator (LINAC) was modeled. Detailed information regarding the dimensions and construction materials of the LINAC head were obtained under a nondisclosure agreement with Elekta AB, Stockholm, Sweden.

To validate the modeled LINAC geometry, we calculated the dose using a 3D voxelized water phantom with dimensions of 40 cm × 40 cm × 40 cm. The voxel size was modeled according to the recommendations provided by the AAPM-168 report[22] and the AAPM-105 report.[23] The dose was calculated as the mean absorbed energy over the mass of each voxel. This includes the X-ray dose as well as the dose from contamination particles resulting from the 18MV beam. The voxel size chosen aligns perfectly with guidelines established in the literature, taking into account the specific attributes of the ionization chamber used for the measurements-the IBA CC13 ionization chambers having a cavity diameter of 6.0 mm and a length of 5.8 mm. To ensure complete coverage of the dose distribution and accurate capture of rapid variations, particularly in the build-up region, we adopted a voxel size of 0.5 cm × 0.5 cm × 0.1 cm along the X, Y, and Z axes, respectively.

Monte Carlo validation

To establish the accuracy and reliability of Monte Carlo simulations carried out using the G4 Linac_MT code under 18MV conditions, a set of experimental measurements was conducted within a water phantom. The aim was to compare depth and lateral dose distributions. For this purpose, IBA CC13 ionization chambers (IBA Dosimetry, Schwarzenbruck, Germany) were utilized in conjunction with a Blue Phantom^2 water phantom. Data acquisition was carried out using myQA Accept 9.0, a sophisticated software package with advanced interface and capabilities.[24-26] It provides a range of tools for accurate data acquisition, facilitating comparison of measured data with extracted reference data, as well as dose manipulation and analysis in single plans and subsets of plans. The software is compatible with any TPS exporting in DICOM format. In particular, it supports 3D visualization of dose cubes, enabling comprehensive dose analysis.

To facilitate meaningful comparisons, both simulated and measured doses were normalized with respect to their individual maximum values. Discrepancies between the Monte Carlo simulations and the experimental measurements were assessed through the utilization of the mean absolute error (MAE)[27] as well as the gamma index (with criteria set at 2% dose difference and 2 mm distance-to-agreement).[28]

The gamma index method assesses dose agreement by simultaneously evaluating the dose difference and spatial positioning between measured and simulated dose distributions. Specifically, it combines the criteria of dose difference (2%) and distance-to-agreement (2 mm) into a single metric that reflects both the accuracy of dose delivery and its spatial precision. A gamma index value of ≤1 indicates that the dose at a particular point meets the specified criteria, showing good agreement between the simulation and measurement. Conversely, values >1 indicate areas where the simulation does not meet the established criteria, highlighting discrepancies in dose distribution. Using both the gamma index and the MAE, we have evaluated the accuracy of the simulation results. The gamma index captures localized doses and spatial discrepancies, particularly in high-gradient areas, while the MAE provides an overall measure of dose differences.

ICRP adult male phantom

To quantify neutron dose distribution in high-energy photon treatments, particularly in prostate radiotherapy, we conducted a simulation study using the Monte Carlo code G4 Linac_MT.[19] We evaluated three treatment plans: 3D-CRT with four fields, 3D-CRT with five fields, and 3D-CRT with seven fields. The ICRP110 phantom studied was precisely engineered to reflect the anatomical and radiological properties of an adult male, based on the chemical compositions and tissue densities stipulated by ICRP110 standards.[18]

The adult male ICRP phantom was voxelized in 3D to create a voxel matrix with dimensions 254 × 127 × 444. A full description of this phantom is provided in Table 1, including mass, volume, dimension, and number of organs modeled. The depiction of the ICRP adult male phantom is illustrated in Figure 1, depicting various views, including coronal, sagittal, transverse, and a full 3D view.

We analyzed the impact of neutron dose in a prostate treatment scenario by employing an 18 MV photon beam, directed through three distinct treatment plans. Neutrons were captured through a phase space situated on the surface of the ICRP adult male phantom. The chosen treatment fields accurately represented the standard configurations employed in the majority of practical prostate treatments, with a consistent source-to-surface distance (SSD) of 90 cm. To reduce the statistical uncertainties due to the low neutron flux, we have considerably increased the number of simulated histories, reaching the value of 5 billion. In addition, phase space recycling has been implemented, with the process being run a million times. This approach aims to optimize the distribution of the neutron dose captured in each voxel. The accuracy of the simulations depends on a number of factors, including accurate modeling of the geometry and appropriate use of the initial parameters. The validity of the geometry is confirmed by experimental data on the photon dose distribution, reinforcing the reliability of our results.

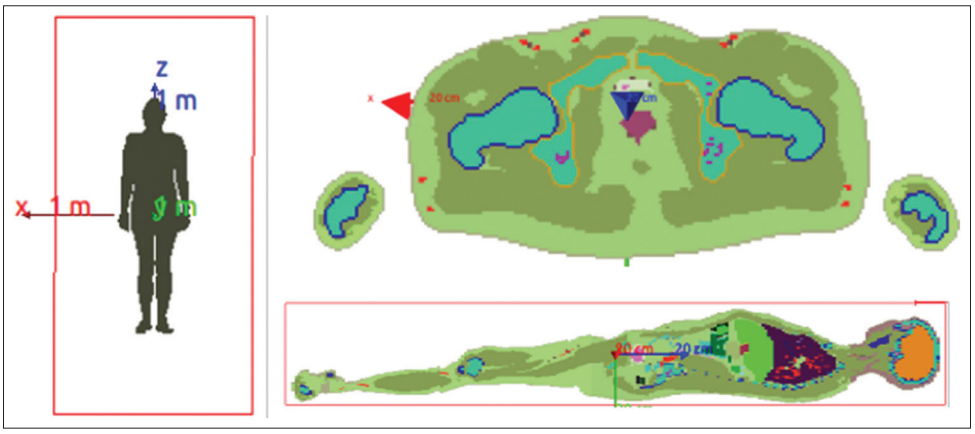

Figure 1: Graphical representation of an ICRP adult male phantom presented in coronal, sagittal, and three-dimensional views

Results and Discussion

Validation of Monte Carlo simulations by experimental measurements

Experimental measurements of the depth and lateral dose distribution in a water phantom were used to validate the accuracy of the G4 Linac_MT code model for the Elekta accelerator head. To achieve a high degree of correspondence with the experimental measurements, the initial parameters of the Gaussian beam electrons have been optimized.[29] These electrons are accelerated by a voltage of 18 MV to generate X-rays by collision with the target material. The electrons modeled have a mean energy of 15.6 MeV, a sigma energy of 0.4 MeV, and a spot size of 0.5 mm.

The validation of the Monte Carlo simulations through experimental measurements of the depth and lateral dose in a water phantom is presented in Figure 2. The phantom was irradiated at a SSD of 90 cm using irradiation fields of 2 cm × 2 cm, 10 cm × 10 cm, and 30 cm × 30 cm. Figure 3 displays the uncertainties of the dosimetric calculations.

Table 1: ICRP male adult phantom: Body composition and voxel characteristics

phantom parameters	Value
Body masse (kg)	73.3
Body volume (cm^3)	2.62E05
Number of phantom organs	139
Total number of voxels	14,322,552
Number of voxels in XYZ	254×127×444
Phantom dimension XYZ (mm^3)	542.798×271.399×1776

ICRP: International commission on radiological protection

Table 2 presents the gamma index percentages (2%/2 mm) and the MAE of the comparison between the Monte Carlo simulations and experimental measurements.

The measurements of the Monte Carlo simulations and experimental measurements of the depth and lateral dose were very similar, as shown in Figure 2, which indicates the high accuracy of the G4 Linac_MT code. Table 2 further supports this conclusion, with the mean absolute dose error and gamma index (2%/2 mm) indicating that all simulated dose results agree with the experimental measurements within an error of <0.93%.

Statistical uncertainties are <2% in all MC calculations, while statistical uncertainties for depth dose distributions increase with depth due to the exponential attenuation of photons.[30,31] It is also noted that the statistical uncertainties increase in the build-up region due to the disturbance of the contamination particles that appear with the photon beam in this region.[32,33] For the dose profiles, the statistical uncertainty increases in the region outside the irradiation field, which is explained by the fact that the photon flux reaching the edges of the jaws collimator is low compared to the middle of the field.[30] The geometry of the LINAC Elekta Synergy modeled in 18MV mode is also validated for other radiation fields presented in our recently published study.[29]

Neutron production

The 18 MV photon beam is typically used to irradiate deep-seated tumors.[34] These high-energy beams are accompanied by the appearance of other particles created by the interaction of the X-rays with obstacles when the photons are collimated toward the surface of the radiation field.[12,35] The contaminating particles that appear with photon beams

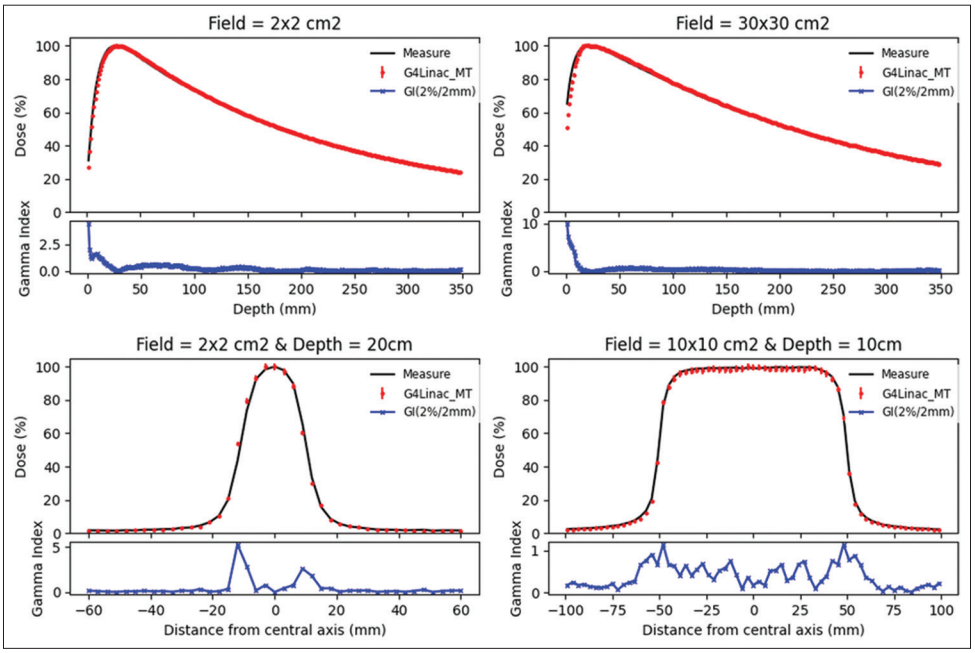

Figure 2: Comparison of the depth (top) and lateral (bottom) dose simulated by the G4Linac_MT code with experimental measurements for the irradiation fields: 2 cm × 2 cm, 10 cm × 10 cm, and 30 cm × 30 cm

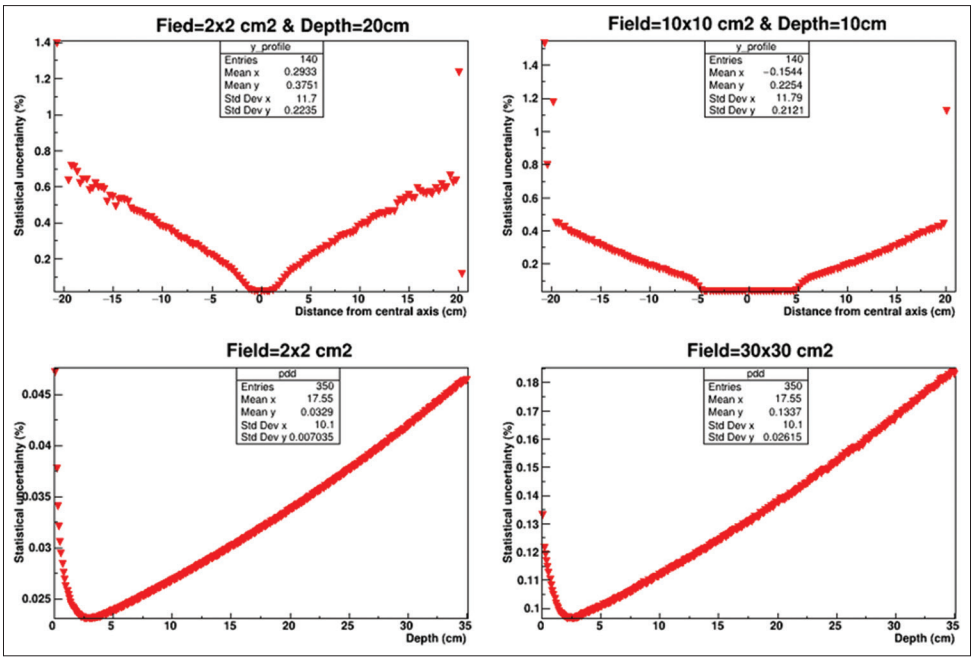

Figure 3: Evolution of statistical uncertainties with the calculated data points associated to the dosimetric functions of the profile dose and PDD

Table 2: Mean absolute dose error and gamma index (2%/2 mm) for depth dose distribution and lateral dose in different field sizes

Beam	Fields	Gamma index (%)	MAE (%)
PDD	2 cm × 2 cm	96.26	0.78
	30 cm × 30 cm	96.85	0.74
Profile	2 cm × 2 cm and depth=20 cm	90.24	0.93
	10 cm × 10 cm and depth=10 cm	97.01	0.78

PDD: Depth dose distribution, MAE: Mean absolute error

are generally electrons and positrons that are created by the Thomson–Rayleigh effect, photoelectric effect, Compton effect, and pair creation effect.[36] Moreover, the electrons and positrons created have enough energy to create ionization when they interact with different elements of the LINAC or with patient's body during the deposition of the photon dose. 18 MV photon beams are also characterized by the presence of neutron and proton contaminants. These particles are created by photonuclear reactions between high-energy photons (typically >8 MeV) and materials with a high photonuclear cross section, such as high-Z materials used in linac components.[13,35,37] Photonuclear reactions occur when the energy of the incident photon exceeds the binding energy per nucleon within the nucleus, typically >8 MeV, which is why these reactions are not observed at lower photon energies. In practical radiotherapy treatments, these particles are not planned by the TPS,[9,10] but they contribute to the total dose induced by the 18 MV photon beam.

Using Monte Carlo simulation, we can quantify and evaluate the neutrons produced by 18 MV radiation. In addition, we can track the origin of each type of particle created during the interaction process between the particles and the material. The construction materials for each element in the LINAC head are presented in Table 3. The results illustrated in Figure 4 clearly show that neutron production by photoneutron reaction in LINAC components is directly associated with regions characterized by high material density. This increased density enhances the probability of interactions with a larger number of target nuclei per unit volume, leading to a higher probability of particle interactions and subsequent neutron production.[13] The main process behind neutron production is the (gamma, *n*) reaction, in which high-energy photons, generally in excess of 8 MeV, collide with nuclei of matter, resulting in the emission of neutrons.[37] The relationship between neutron production and material density can be described by the following equation:

$$N = \Phi \cdot \Sigma \quad (1)$$

where:

N is the neutron production rate (number of neutrons per unit time),

Φ is the particle flux (number of incident particles per unit area per unit time).

Σ is the macroscopic cross section for neutron production, which is the probability per unit path length that a neutron interaction will occur (cm^{-1}). The macroscopic cross section Σ can be expressed as:

$$\Sigma = n \cdot \sigma \quad (2)$$

σ is the microscopic cross section for neutron production (barn).

n is the number density of target nuclei.

The results presented in Figure 4 show that the majority of neutrons passing through the phase space come from the

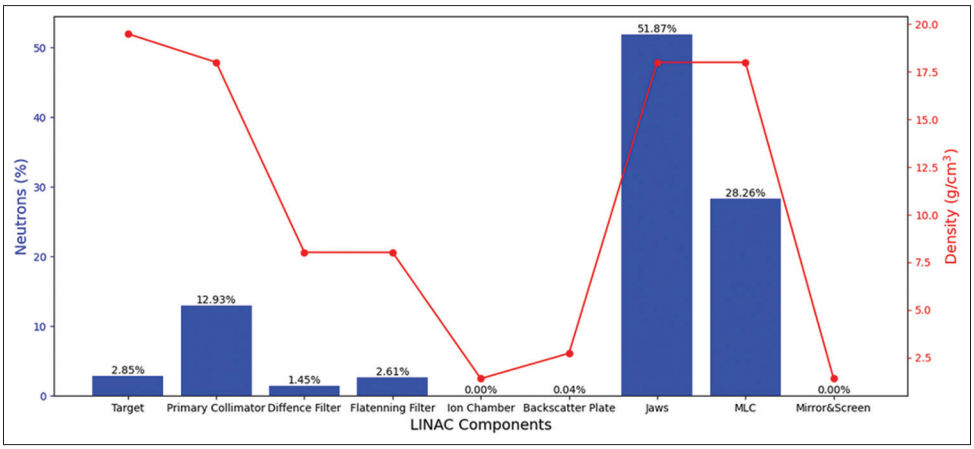

Figure 4: Neutron production percentage across LINAC components and corresponding densities. The blue histogram represents the percentage of neutrons generated within individual LINAC components. These percentages are calculated based on the total neutron count collected within a phase space plane located at 100 cm from the target and for an open irradiation field of 10 cm × 10 cm. The red curve illustrates the density profile of each LINAC component

Table 3: Material composition of Elekta Synergy linear accelerator construction alloys: Classified by abundance

LINAC component	Element composition
Target	Tungsten/rhenium alloy
Primary collimator	Tungsten/nickel/iron alloy
Difference filter	Iron/chromium/nickel alloy
Flattening filter	Iron/chromium/nickel/manganese alloy
Ion chamber	Mylar
Backscatter plate	Aluminum/iron/silicon/magnesium alloy
Jaws	Tungsten/nickel/iron alloy
MLC	Tungsten/nickel/iron alloy
Mirror and screen	Mylar

LINAC: Linear accelerator, MLC: Multi-leaf collimators

secondary collimators (jaws) and multi-leaf collimators (MLC), accounting for around 80% of the total neutron flux. The fact that neutron production is lower in the target despite its high density is due to the fact that photons are created in the target, and a very small percentage of photons can re-enter the target. In the case of the primary collimator, there are two reasons why the percentage of original neutrons in the primary collimator does not exceed 15% in phase space. The first reason is that the collimator is further away from the phase space, making it more likely that neutrons will be scattered laterally. The second is the possibility of neutron absorption in other LINAC components, preventing neutrons from the primary collimator from reaching the phase space placed 100 cm from the target.

Neutrons originating from the secondary collimators have the potential to reach patients during 18 MV beam treatments. Figure 5 provides a visual representation of the quantification of neutrons detected relative to photons, describing their distribution in phase space positioned 100 cm from the target and exposed to a field size of 10 cm × 10 cm. The figure offers a comprehensive analysis of particle dynamics in phase space, focusing specifically on the orientation of neutrons and photons using the direction parameter ϕ, the spatial distribution of neutrons and photons as a function of radial position, energy distribution and intensity of neutrons and photons spectrum.

The neutrons produced in the LINAC head detected at 100 cm from the target are classified by energy ranging from 0.005-2.98 MeV. Among them, 87.05% are intermediate neutrons and 12.95% are fast neutrons. Although we recognize the potential existence of neutrons with energies in excess of 2.98 MeV, our study focuses primarily on neutrons that effectively reach the patient's body. For this reason, the detection and classification processes take place at an SSD of 100 cm. The energy distribution of these neutrons can be explained by taking into account the influence of photons reaching the jaws and the MLC [representing 80% of the origin of detected neutrons, as shown in Figure 4]. These photons undergo an energy loss when passing through the flattening filter and the difference filter, which affects the energy of neutrons generated by photon–neutron reactions. For the neutrons generated in other LINAC components, notably, the primary collimator, are more energetic and can exceed 2.98 MeV, but these neutrons are created far from the irradiation field opening, and probably diffuse laterally or lose some of their energy before reaching the patient. This detected neutron energy is sufficient to cause damage, neutrons whose energy is between 100 keV and 2 MeV are 20 times more dangerous than photons and electrons.[12] Neutrons are uncharged particles, and their ionizing effects result primarily from the secondary charged particles produced during their interactions with matter, such as protons, alpha particles, and recoil nuclei. These secondary particles are characterized by high LET, contributing to the increased relative biological effectiveness (RBE) of neutron radiation.[38,39] The track-averaged LET (LET_t) for these secondary charged particles can be expressed by the following equation:

$$LET_t\left(keV/\mu m\right) = \frac{\sum \Phi_i . LET_i}{\sum \Phi_i} \quad (3)$$

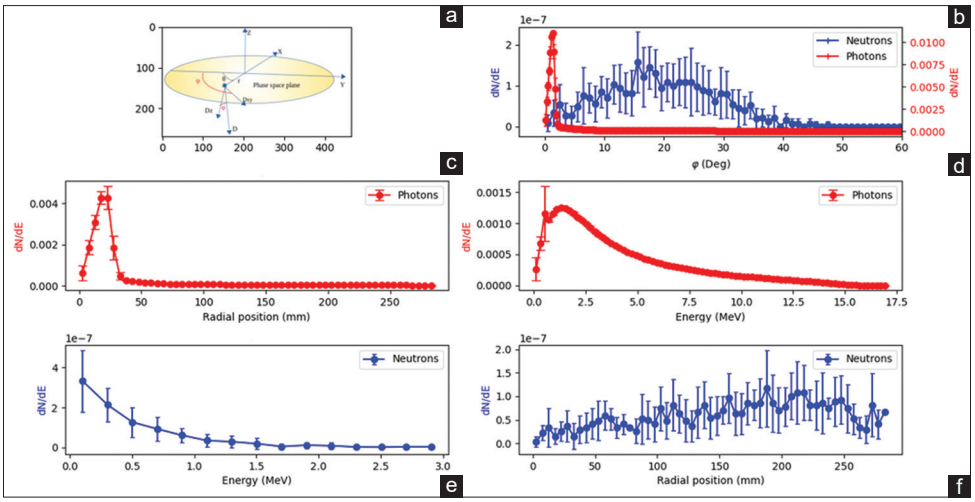

Figure 5: Particle dynamics in the phase space for photons and neutrons. Phase space is a file which stores information such as position, kinetic energy, direction cosine, particle type, and weight of the particle across a surface. (a) Position and Direction: Particle positions are characterized by angles θ and radial distance r from the origin, while their direction is represented by angles ψ and ϕ. The vector D comprises Dxy (azimuthal component) and Dz (vertical component). (b) Direction Parameter ϕ: Examining the orientation of neutrons and photons using the direction parameter ϕ. (c and f) Radial Distribution: Investigating the spatial distribution of neutrons and photons as a function of radial position. (d and e) Spectrum: Analyzing the energy distribution and intensity of neutrons and photons through their spectrum

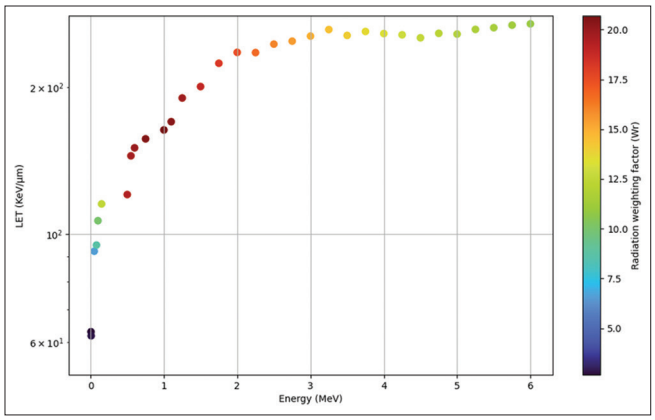

Figure 6: Linear energy transfer values in water are illustrated for a range of neutron energies from 0.005 MeV to 6 MeV. The graph also presents the corresponding weighting factor (Wr) calculated using equation (3) recommended by ICRP103

Where Φ_i represents the fluence of charged particle *i*, and the stopping power LET_i is expressed by the equation (4):

$$LET_i\left(keV/\mu m\right) = dE_i/dx \quad (4)$$

where dE_i is the energy lost by the particle and *dx* is the distance traveled in the medium.

In 2007, the ICRP introduced a major update to the radiation weighting factors (W_r) to reflect the biological effectiveness of different types of radiation.[40] These factors are used to calculate the dose equivalent and the effective dose, accounting for the differences in biological impact. For most radiation types, including photons and electrons, W_r is set at a constant value, independent of energy. However, for neutrons, W_r varies with energy, reaching approximately a value of 20 for neutrons with an energy of around 1 MeV. For high-LET radiation, such as neutrons and alpha particles, W_r reflects the increased potential for biological damage compared to low-LET radiation, such as photons and electrons, which cause less ionization over the same distance.[40] The mathematical expression defining the radiation weighting factors for neutrons is presented below (5):

$$W_r = \begin{cases} 2.5 + 18.2e^{-\left[ln(E_n)\right]^2/6} & for E_n < 1MeV \\ 5 + 17e^{-\left[ln(2E_n)\right]^2/6} & for 1MeV \le E_n \le 50MeV \end{cases} \quad (5)$$

To clarify the LET of neutrons produced in the LINAC 18 MV geometry, Figure 6 shows LET values in a water medium for a neutron energy spectrum ranging from 0.005 MeV to 6 MeV. It also illustrates the corresponding weighting factor (W_r) derived from the equation (5). Our approach involved calculating the LET for each step within the water phantom by summing the energy deposited across all steps within an event and subsequently dividing it by the cumulative track lengths.

The most significant weighting factor is associated with neutrons having an energy of approximately 1 MeV, recording a W_r of 20.7. In other words, these neutrons have a biological impact approximately 20.7 times higher than that of electrons and photons. This observation is supported by Baiocco *et al*.,[41] who demonstrate that neutrons with energy close to 1 MeV exhibit higher levels of RBE.

Beyond 2 MeV of neutron energy, the LET begins to stabilize, with the weighting factor converging to approximately 10 in the 2 MeV to 20 MeV range. This approximation is based on calculations performed in 5 keV increments, where W_r remains consistently around this value. Furthermore, for low-energy neutrons below 10 keV, the weighting factor starts at 2.5 and gradually increases to 5 as the energy reaches 100 keV.

Neutron dose

The detected neutrons are recorded and stored in a phase space database placed at 100 from the target. This phase space is a file which stores information such as position, kinetic energy, direction cosine, particle type, and weight of the particle across a surface. This recorded data is then used for dose calculation, where the neutron contribution is filtered using the PDG particle identification code to determine their type. Our study aimed to quantify the neutron dose in comparison to the total dose within a water phantom irradiated by an 18 MV LINAC, with a fixed field size of 5 cm × 5 cm at the central axis of the beam. The comparison of these dose distributions is depicted in Figure 7a. Furthermore, our investigation delved into the ability of detected neutrons to penetrate various materials and explored their absorption characteristics when exposed to an 18 MV photon beam, as illustrated in Figure 7b and c. Specifically, we examined the depth dose distribution in different media, highlighting the deposition of neutron contamination dose in the irradiated medium.

Materials considered included water (H_2O), lead (Pb), and cadmium (Cd), which are frequently used for neutron shielding purposes.[42,43] In addition, we examined the role of hydrogen (H) in water, investigating its ability to absorb neutrons, thereby delaying their speed and reducing their energy. Hydrogen is an elemental component commonly found in human soft tissues, including (H, 10.5%), carbon (C, 22.6%), oxygen (O, 63.7%), and nitrogen (N, 2.34%).

Based on the results presented in Figure 7, we can observe that the neutron dose initially increases up to a point corresponding to the maximum dose, and then decreases exponentially as the depth of the medium increases. The neutron dose contribution in water can reach a maximum of 1.1% near the surface of the phantom, decreasing exponentially with increasing depth. This phenomenon is attributed to water's powerful moderating effect on neutrons, particularly low-energy neutrons (87.05% of detected neutrons are classified as intermediate neutrons). The high probability of neutron deceleration in water leads to an increase in dose deposition. However, as depth increases, the proportional abundance of neutrons decreases, resulting in a lower contribution to the total dose. These results also demonstrate the influence of material properties on neutron dose distribution. It is particularly interesting to note that at the material surface, the absorbed dose is higher for water and cadmium than for carbon and lead. This difference in neutron absorption can be attributed to the inherent properties of each material.[44] The unique properties of materials such as water, characterized by the presence of hydrogen, contribute to a higher neutron collision cross section in the energy range from 0.005 MeV to 3 MeV (the range of neutrons detected).[45] A high neutron cross section in a material increases the probability of interactions between neutrons and atomic nuclei, leading to a reduction in neutron path length and a high neutron dose deposition. Conversely, materials with lower neutron cross sections facilitate neutron travel distances before absorption. In particular, high-density substances such as lead have comparatively lower neutron cross sections than water, carbon, and cadmium. As a result, the probability of neutron absorption is reduced compared to these materials.

To illustrate the relationship between neutron cross-section and material interaction, the concept of the probability function P (x) is useful. This function describes the probability of a neutron undergoing an interaction at a specific depth (x) in a given medium. This neutron flux represents the number of neutrons passing through a designated zone per unit of time. The probability that a neutron can traverse a distance (x) within a material medium without experiencing any interaction is governed by the equation:

$$P(x) = e^{(-\Sigma x)} \quad (6)$$

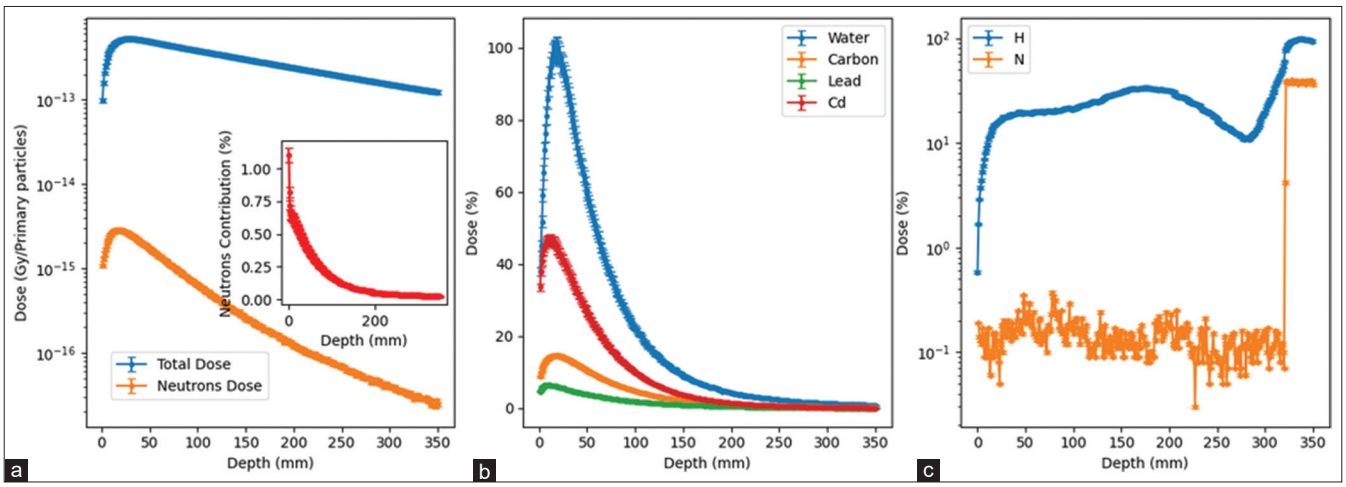

Figure 7: Neutron dose contribution and neutron depth dose in different media. (a) Comparison of neutron dose contribution to total dose in a water phantom irradiated by an 18 MV LINAC with a 5 × 5 cm² field size at the central axis of the beam. (b and c) Investigation of neutron penetration and absorption characteristics in various media. (d) Neutron dose contribution in water compared with total dose from an 18 MV LINAC beam. Depth dose distributions depicted for water (density: 1 g/cm3), carbon (density: 2.2 g/cm3), lead (density: 11.4 g/cm3) Cadmium (density: 8.65 g/cm3), Hydrogen (density: 0.084 mg/cm³), and Nitrogen (density: 1.165 mg/cm³)

The macroscopic cross section (Σ) is related to the microscopic cross section (σ) and the atom number density (N) by equation (2).

We can deduce the probability of the neutron interacting with matter nuclei by the quantity *P* (x) dx:

$$P(x)dx = e^{(-\Sigma x)}.\Sigma dx \quad (7)$$

Using the expression provided in equations (6) and (7), we can determine the mean free path covered by a neutron between successive collisions. This value corresponds to the mean free path and is obtained by evaluating the average distance x that a neutron traverses without experiencing any interactions, across the entire distribution of interaction probabilities. We, therefore, deduce the mean free path equal to the inverse of the macroscopic cross section, we express it in centimeters:

$$\lambda = \frac{1}{\Sigma} \quad (8)$$

For water, the relatively higher macroscopic cross-section (Σ) stems from its hydrogen composition [Figure 8]. Consequently, the mean free path for neutrons in water is shorter compared to lead.

In equation (6), the exponential term will be lower for water due to its higher Σ. This signifies that the probability of neutron travel without interactions at a certain depth (x) is greater for lead in comparison to water.

In Figure 8, we have provided a representation of the cross-sectional profiles for eight selected materials, effectively demonstrating the various interactions that LINAC 18 MV neutrons undergo within these materials. The figure highlights the neutron processes in the constitution of the total cross section. This visual representation highlights the ability of neutrons from the 18 MV photon beam originating from the medical accelerator to penetrate the LINAC shielding and the patient's body during treatment.

Neutron dose contribution during prostate treatment

The objective of this study is to quantitatively assess the neutron dose contribution during the treatment of prostate tumors using an 18 MV photon beam. In addition, the study aims to compare the neutron contribution across different treatment plans. Specifically, three distinct treatment plans are investigated: 4-field 3D-CRT, 5-field 3D-CRT, and 7-field 3D-CRT.

Figure 9 presents a visual representation of the dose heat map in a two-dimensional slice for each of the aforementioned treatment plans using an 18 MV photon beam. In the context of the 4-field 3D-CRT plan, the prostate receives irradiation from two lateral angles positioned at 90° and 270°, as well as an anterior angle at 0° and a posterior angle at 180°. In the 5-field 3D-CRT approach, the prostate is irradiated from four lateral angles situated at 60°, 120°, 240°, and 300°, accompanied by an additional anterior angle at 0°. In the case of the 7-field

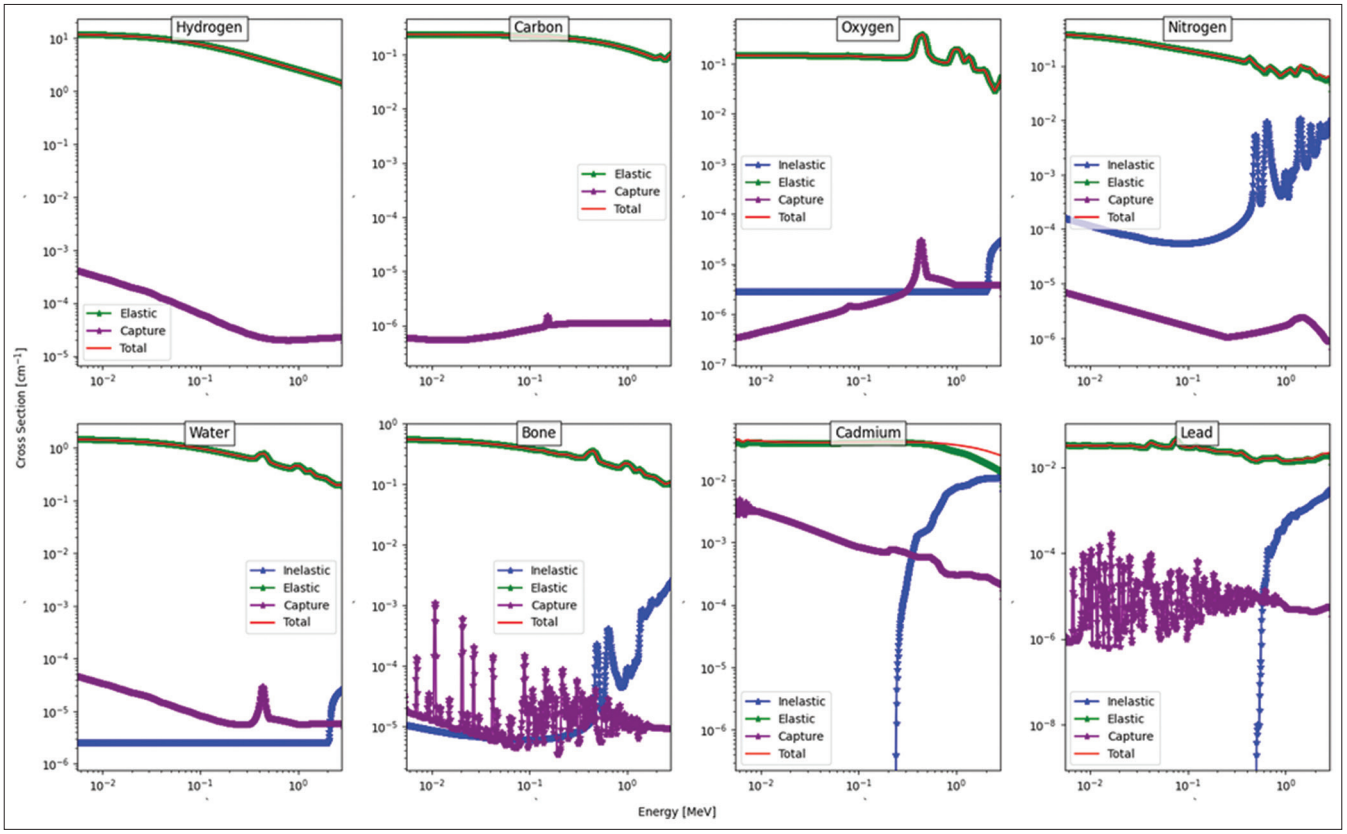

Figure 8: Cross section of materials over a neutron energy range from 0.005 MeV to 3 MeV. This representation illustrates the cross-section associated with individual neutron processes, as well as the total combined cross-section. This data is extracted from MC Geant4 and the NIST database

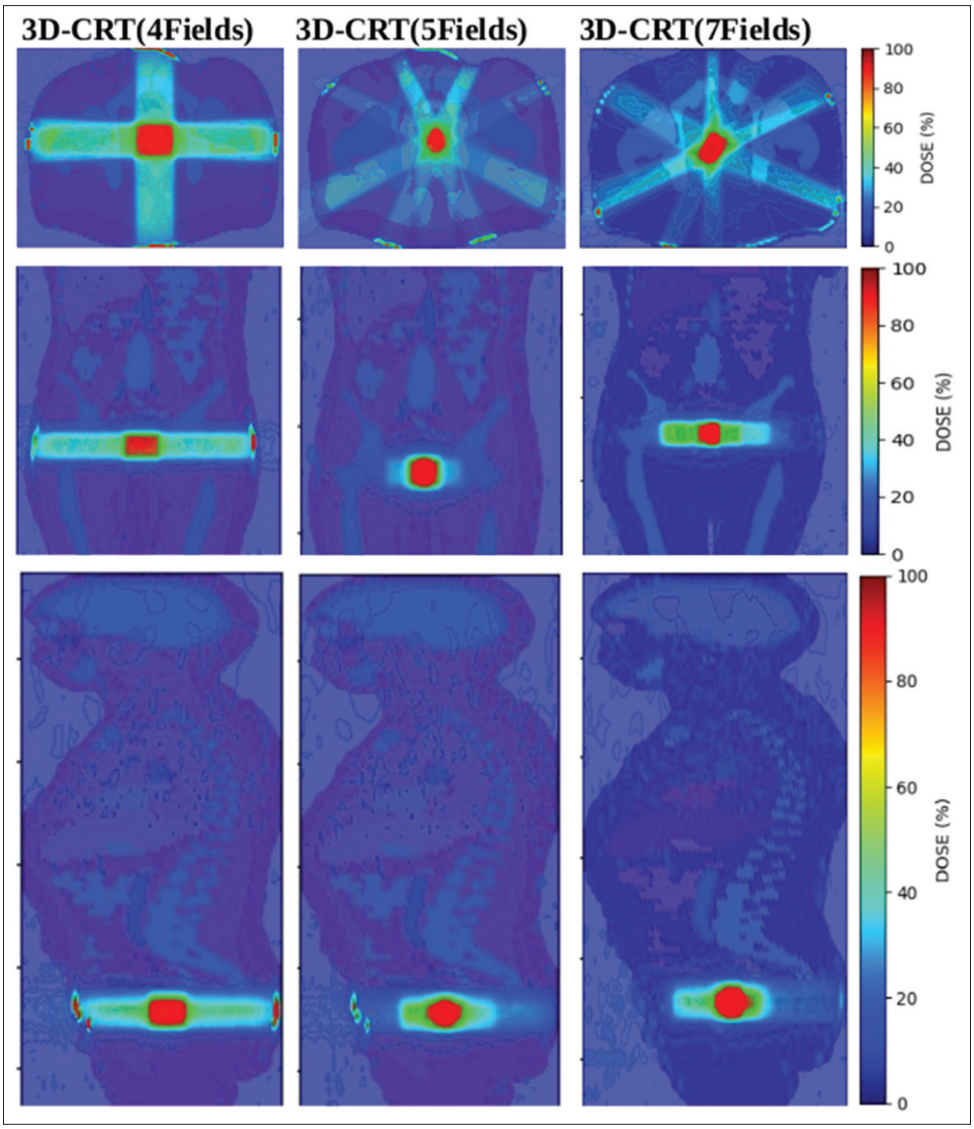

Figure 9: Comparison of prostate cancer treatment plans in the ICRP adult male phantom. The visualization represents dose distribution maps for different treatment plans in different views, including coronal, sagittal, and transverse planes. Left image: three-dimensional (3D) conformal plan with 4 fields, Middle image: 3D conformal plan using 5 fields, Right image: 3D conformal plan using 7 fields. Across all scenarios, a uniform field size of 7 cm × 7 cm is maintained

3D-CRT, the gantry angles are projected at 35°, 80°, 140°, 180°, 220°, 280°, and 325°. The map view provides a clear illustration of the spatial distribution of radiation dose in the prostate region.

To accurately assess the contribution of neutrons to the overall deposited radiation dose, we performed an analysis of the dose distribution in each organ of the ICRP adult male phantom [Figure 10]. To achieve this objective, the irradiation fields are filtered by other particles and only the neutron sources collected with the 18 MV beam are introduced into the treatment plans to precisely quantify the neutron dose fraction in relation to the overall dose.

Quantifying organ-specific doses makes it possible to visualize the impact of neutrons in each treatment plan.

In Figure 10, we have highlighted the organs with sufficient neutron flux, focusing on those where the statistical uncertainty in the Monte Carlo dose calculation remains below 2%. An important observation drawn from the outcomes depicted in Figure 10 is the distinct decrease in neutron dose contribution in each organ for the 3D-CRT treatment plan (5 fields) compared to the 3D-CRT (4 fields) and 3D-CRT (7 fields) treatment plans. Moreover, a significant convergence of neutron contributions becomes evident between the 3D-CRT (4 fields) and 3D-CRT (7 fields) modalities in all organs shown in Figure 10.

It is also clear that neutrons exert a significant influence on the overall dose in organs located at a distance from the irradiation fields. This is due to the predominant generation of neutrons in the secondary collimators and the MLC [Figure 4]. As a

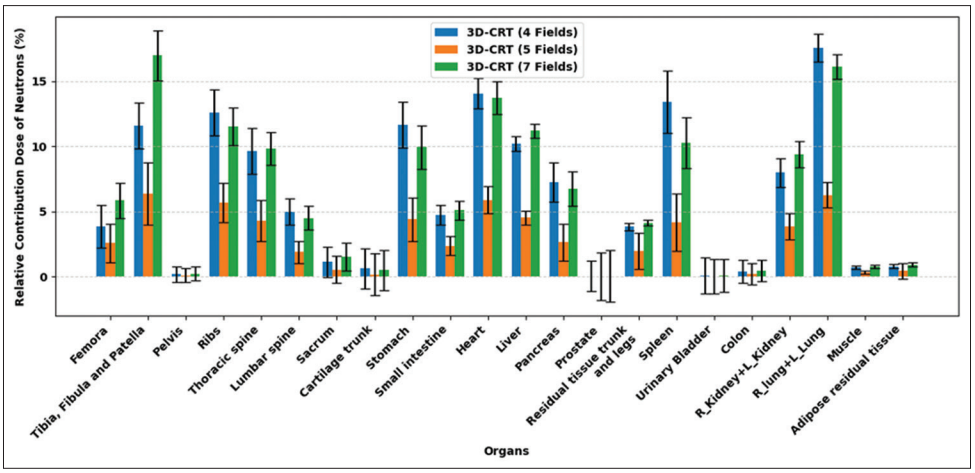

Figure 10: Neutron dose contributions across various organs and body regions for three treatment plans: Three-dimensional conformal radiotherapy (3D-CRT) (4 Fields), 3D-CRT (5 Fields), and 3D-CRT (7 Fields). The percent dose contribution is graphically depicted for each treatment plan, accompanied by uncertainty dose errors illustrated as bars

result, these neutrons exhibit a higher lateral dispersion, a feature highlighted by their radial positioning illustrated in Figure 5. The neutron dose fraction remains minimal in the prostate and bladder, which is explained by the high photon dose prevailing in the irradiation fields. Conversely, it should be noted that neutrons exert a more significant influence in body regions with abundant bone structures, notably the ribs, femur, tibia, fibula, patella, and spine. The increased contribution observed in bone regions can logically be attributed to the dense composition of bone materials, which consequently increases neutron dose deposition.

The collective neutron dose contribution to all body regions except organ contents amounts to 0.63%, 0.33%, and 0.77% for the corresponding treatment plans of 3D-CRT (4 fields), 3D-CRT (5 fields), and 3D-CRT (7 fields). The diminished neutron contribution in the 3D-CRT (5 fields) approach can be rationalized by the omission of the posterior field and the utilization of lateral fields inclined at a 60° angle, strategically avoiding irradiation of the spine and femurs.

Neutron-specific absorbed fractions (SAFs)

Neutron emissions from high-energy photon beams, such as those produced by an 18 MV LINAC, pose a significant challenge in radiotherapy due to their high LET and RBE, both of which are considerably higher than those of photons. Unlike other secondary particles, neutrons can penetrate deep into tissues, depositing energy and causing substantial biological damage even at low doses. Studies, including Assalmi and Diaf,[11] have demonstrated that secondary neutrons generated from the LINAC head are capable of depositing doses both within and outside the primary irradiation field. Their results also indicated that neutron energies can reach up to 0.5 MeV in organs such as the lung and trachea during scenarios such as breast treatment, highlighting the deep tissue penetration capability of these particles. In this study, we focus on estimating the potential biological implications and radiation dose distributions for various organs and tissues.

This investigation specifically addresses the underestimated internal dosimetric impact of neutron radiation by calculating specific absorbed fractions (SAFs)[46] for neutron energies ranging from 0.005 MeV to 3 MeV. This factor is commonly used in radiation dosimetry to estimate the absorbed dose in different organs and tissues due to the interaction of ionizing radiation.[46,47] Although SAFs are generally used in internal dosimetry to quantify the ratio of energy absorbed in a target tissue to the energy emitted by a source, we used it in this study to evaluate self-irradiation scenarios-specifically, to quantify how much energy can be absorbed by each organ-at-risk, based on the scenario where neutrons of these energy levels reach the organ. This approach allows us to assess the absorbed energy within target organs, such as the pancreas, liver, spleen, and prostate, when exposed to neutron energies.

The evaluation of specific absorbed fractions (SAF) is carried out using the InterDosi code,[48] with a simulation of 3.10^8 histories numbers. We have validated this code using electron and photon particles against the reference data provided by the OpenDose collaboration.[49] This validation process encompasses scenarios where the four identified organs experience self-irradiation from electrons and photons with energies of 1 MeV and 2 MeV. The results of this validation are presented in Table 3, where a comparison is made between our outcomes and the reference results calculated by the GATE code. This comparative analysis allows us to evaluate the alignment and agreement between our findings and established benchmarks, thereby enhancing the credibility and significance of our results.

According to the results detailed in Table 4, the results obtained by Monte Carlo calculations using the InerDosi code show good agreement with the corresponding reference values. This agreement is particularly strong, with deviations of < 0.37% and 0.73% for electrons and photons, respectively. This low deviation underlines the high degree of confidence in the reliability and accuracy of our research results.

The study of specific absorption fraction (SAF) calculations on neutrons generated by a medical linear accelerator operating in 18 MV mode is presented visually in Figure 11. In this figure, SAFs are shown as a function of energy, covering the range from 0.005 MeV to 3 MeV. The figure further explains the interaction between SAFs and the mass and density of each separate target organ.

The main observation arising from the SAF results presented in Figure 11, specifically concerning the self-irradiation of the four organs, is as follows: for all organs, there is a decrease in SAF values as neutron energy increases. An exception can be noted in the case of the prostate at 0.5 MeV, where a minor increase occurs, as well as in the lungs, where SAF shows a slight increase at 3 MeV compared to 2.5 MeV. We also observe that the decreasing rate of SAF gradually stabilizes as energy increases. The reason for these effects can be attributed to fluctuations in neutron cross section in the organ materials, as shown in Figure 8. Indeed, the prostate, despite having a lower mass compared to other organs, has higher SAF values, calculated as the ratio of energy absorption per organ mass. Consequently, SAF values among the four studied organs are inversely correlated with their masses. This principle can be extrapolated to the majority of other organs specifically, organs with lower mass have relatively higher SAF values. This underlines the importance of organ-specific characteristics in neutron dosimetry assessments. It is important to note that higher SAF values do not necessarily indicate greater energy absorption within the organ. Figure 12 illustrates the ratio between energy absorbed and energy emitted within the organ. Notably, higher absorption rates are observed in the kidneys and lungs. This can be attributed to the larger volumes of these organs, leading to increased interaction with emitted neutrons and subsequently greater energy deposition. The situation is especially marked in the case of bladders, where we have simulated the urinary bladder wall. Absorption rate also decreases as neutron energy increases, indicating that the probability of neutrons passing through the material without energy deposition also increases, due to the cross section [Figure 8].

Conclusion

This study explores the impact of photo–neutron doses from neutrons in an 18 MV medical linear accelerator. Using advanced Monte Carlo simulations, we have investigated in detail the presence, characteristics, and impact of photoneutrons in prostate treatment scenarios. The accuracy of the Monte Carlo simulations was validated by experimental measurements, showing a high level of agreement between simulated and measured dose distributions. This high agreement confirms the reliability of our simulation approach, which enables us

Table 4: Self-irradiation specific absorption fractions within an ICRP adult male phantom for monoenergetic electrons and photons at 1 MeV and 2 MeV: Comparative analysis with OpenDose collaboration reference data calculated using the GATE Monte Carlo code

Energy (MeV)	Organ	Electrons			Photons		
		This study	OpenDose	Difference (%)	This study	OpenDose	Difference (%)
1	Liver	0.53567	0.53545	0.04	0.08422	0.08373	0.59
	Prostate	50.41720	50.35680	0.12	1.83477	1.82498	0.54
	Spleen	6.14346	6.13766	0.09	0.43719	0.43442	0.64
	Pancreas	6.55266	6.54770	0.08	0.44889	0.44563	0.73
2	Liver	0.51588	0.51540	0.09	0.06867	0.06857	0.15
	Prostate	42.52580	42.36915	0.37	1.31932	1.31316	0.47
	Spleen	5.64226	5.62824	0.25	0.33949	0.33909	0.12
	Pancreas	5.95798	5.94232	0.26	0.34742	0.34687	0.16

SAFs are expressed in kg^{-1}. SAFs: Specific absorbed fractions, ICRP: International commission on radiological protection

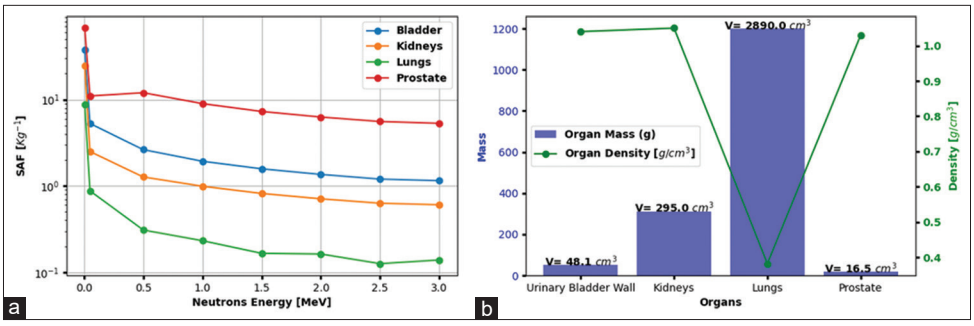

Figure 11: Analysis of the specific absorption fraction (SAF) for neutrons emitted by the 18 MV LINAC. (a) SAFs in relation to energies ranging from 0.005 MeV to 3 MeV are presented, which relates to self-irradiation scenarios in the bladder, kidney, lung, and prostate. (b) The figure gives an overview of the mass, volume, and density attributes of the respective organs, to understand their characteristics and their interaction with SAF values

to accurately model real conditions and explore scenarios that are not possible to reproduce experimentally. Neutron penetration and cross-section interaction in various media help us to understand their distribution and potential risks. By quantifying neutron contributions in distinct prostate treatment plans, we provide valuable insights into the interaction between high-energy photon beams and secondary neutrons. Our results demonstrated the decrease in neutron dose contribution in the case of CRT-(5Fileds). In addition, the quantification of specific absorbed fractions in the organs irradiated by the detected neutrons adds a further degree of precision to the assessment of potential organ-specific effects. In particular, the observed decrease in SAFs with increasing neutron energy underlines the importance of neutron considerations in 18 MV beams.

Acknowledgment

We thank Elekta AB, Stockholm, Sweden providing for the geometry of linac Elekta Synergy MLCi2 through a nondisclosure agreement (NDA), and Khalid el Ouardy in the Department of Radiation Oncology Achark Clinic for providing us with the experimental dose data.

This research was supported in part through computational resources of HPC-MARWAN (www.marwan.ma/hpc) provided by the National Center for Scientific and Technical Research (CNRST), Rabat, Morocco.

Financial support and sponsorship

Nil.

Conflicts of interest

There are no conflicts of interest.

References

1. Shirzadfar H, Khanahmadi M. Current approaches and novel treatment methods for cancer and radiotherapy. Int J Biosen Bioelectron 2018;4:224-9.
2. Ahmad SS, Duke S, Jena R, Williams MV, Burnet NG. Advances in radiotherapy. BMJ 2012;345:e7765.
3. De Ruysscher D, Niedermann G, Burnet NG, Siva S, Lee AW, Hegi-Johnson F. Radiotherapy toxicity. Nat Rev Dis Primers 2019;5:13.
4. Chen HH, Kuo MT. Improving radiotherapy in cancer treatment: Promises and challenges. Oncotarget 2017;8:62742-58.
5. Bourhis J, Montay-Gruel P, Gonçalves Jorge P, Bailat C, Petit B, Ollivier J, *et al.* Clinical translation of FLASH radiotherapy: Why and how? Radiother Oncol 2019;139:11-7.
6. Wei S, Lin H, Choi JI, Simone CB 2nd, Kang M. A novel proton pencil beam scanning FLASH RT delivery method enables optimal OAR sparing and ultra-high dose rate delivery: A comprehensive dosimetry study for lung tumors. Cancers (Basel) 2021;13:5790.
7. Bélanger-Champagne C, Roddy D, Penner C, Tattenberg S, Trinczek M, Yen S, *et al.* "Delivery of proton FLASH at the TRIUMF Proton Therapy Research Centre." Nuclear Instruments and Methods in Physics Research Section A: Accelerators, Spectrometers, Detectors and Associated Equipment 2023;1052:168243. Available from: https://doi.org/10.1016/j.nima.2023.168243.
8. Mei Z, *et al.* "Focused Proton Beam Generating Pseudo Bragg Peak for FLASH Therapy." Nuclear Instruments and Methods in Physics Research. Section A, Accelerators, Spectrometers, Detectors and Associated Equipment, 2022;1032:166618. Available from: https://doi.org/10.1016/j.nima.2022.166618.
9. Van Hoey O, Stolarczyk L, Lillhök J, Eliasson L, Mojzeszek N, Liszka M, *et al.* Simulation and experimental verification of ambient neutron doses in a pencil beam scanning proton therapy room as a function of treatment plan parameters. Front Oncol 2022;12:903537.
10. Faghihi Moghaddam F, Bakhshandeh M, Ghorbani M, Mofid B. Assessing the out-of-field dose calculation accuracy by eclipse treatment planning system in sliding window IMRT of prostate cancer patients. Comput Biol Med 2020;127:104052.
11. Assalmi M, Diaf EY. The behavior of the contamination particles appears with the 18 MV photon beam delivered by Elekta Synergy MLCi2. Radiat Phys Chem 2022;199:110384.
12. Banaee N, Goodarzi K, Nedaie HA. Neutron contamination in radiotherapy processes: a review study. J Radiat Res 2021;rrab076. doi: 10.1093/jrr/rrab076.
13. Shojaei M, Rashedi S, Chakoli AN, Karimi AH, Geraily G. Measurement of neutron equivalent dose in the thyroid, chiasma, and lens for patients undergoing pelvic radiotherapy: A phantom study. Appl Radiat Isot 2022;184:110188.
14. Elmtalab S, Shanei A, Choopan Dastjerdi MH, Brkić H, Abedi I, Amouheidari A. Determination of the neutron contamination during brain radiotherapy using a moderated-boron trifluoride detector and the Mcnp Monte Carlo code. Radiat Prot Dosimetry 2022;198:129-38.
15. Tai DT, Loan TTH, Sulieman A, Tamam N, Omer H, Bradley DA. Measurement of Neutron Dose Equivalent within and Outside of a LINAC Treatment Vault Using a Neutron Survey Meter. Quantum Beam Sci 2021;5:33. Available from: https://doi.org/10.3390/qubs5040033.
16. Dowlatabadi H *et al*. Study of Photoneutron Production for the 18 MV Photon Beam of the Siemens Medical linac by Monte Carlo Simulation. J Biomed Phys Eng 2020;10:679-690. doi: 10.31661/JBPE.V0I0.939.
17. Park SH, Kang JO. Basics of particle therapy I: Physics. Radiat Oncol J 2011;29:135-46.
18. Menzel HG, Clement C, DeLuca P. ICRP Publication 110. Realistic reference phantoms: an ICRP/ICRU joint effort. A report of adult reference computational phantoms. Ann ICRP 2009;39:1-164. doi: 10.1016/j.icrp.2009.09.001. Erratum in: Ann ICRP 2009;39:165.
19. EL Bakkali J, Doudouh A, Mansouri H, EL Bardouni T. G4Linac_MT, an easy-to-use Geant4-based code for modeling medical linear accelerator. Radiat Phys Chem 2019;157:65-71.
20. CNRST/HPC-MARWAN , URL : https://hpc.marwan.ma.
21. Assalmi M, Diaf EY, Mansour N. Validation of Monte Carlo geant4 multithreading code for a 6 MV photon beam of Varian linac on the grid computing. Rep Pract Oncol Radiother 2020;25:1001-10.
22. Sechopoulos I, Rogers DW, Bazalova-Carter M, Bolch WE, Heath EC, McNitt-Gray MF, *et al.* RECORDS: Improved reporting of Monte Carlo radiation transport studies: Report of the AAPM Research Committee Task Group 268. Med Phys 2018;45:e1-5.
23. Chetty IJ, Curran B, Cygler JE, DeMarco JJ, Ezzell G, Faddegon BA, *et al.* Report of the AAPM task group no. 105: Issues associated with clinical implementation of Monte Carlo-based photon and electron external beam treatment planning. Med Phys 2007;34:4818-53.
24. Padelli F, Aquino D, Fariselli L, De Martin E. IBA myQA SRS Detector for cyberknife robotic radiosurgery quality assurance. Appl Sci 2022;12:7791.
25. Thanh Tai D, Tuan HD, Xuan Hai N, Ngoc Anh N, Bradley D, Sandwall P, *et al*. Examining Beam Matching in the Commissioning of a Halcyon Accelerator. Nuclear Science and Engineering 2024. p. 1–11. Available from: https://doi.org/10.1080/00295639.2024.2366733.
26. Cho JD, Chun M, Son J, An HJ, Yoon J, Choi CH, *et al*. Efficient Verification of X-ray Target Replacement for the C-series High Energy Linear Accelerator. Prog. Med. Phys 2018;29:92-100. Available from: https://doi.org/10.14316/pmp.2018.29.3.92.
27. Assalmi M, Diaf EY. Monte Carlo simulation of surface dose and dose rate in 6MV-FFF beams. Moscow Univ Phys 2021;76 Suppl 1:S36-5.
28. Hussein M, Clark CH, Nisbet A. Challenges in calculation of the gamma index in radiotherapy – Towards good practice. Phys Med 2017;36:1-11.
29. Assalmi M, Diaf EY. Effect of the Gaussian distribution parameters of the electron beam generated at the target on the simulated x-ray dose. Biomed Phys Eng Express. 2023;9. doi: 10.1088/2057-1976/acbaa0.
30. EL Bakkali J, EL Bardouni T. Validation of Monte Carlo geant4 code for a 6MV Varian linac. J King Saud Univ Sci 2017;29:106-13.
31. Bencheikh M, *et al*. Analysis of stabilization of photon beam softening with off-axis distance for filtration system enhancement to increase

dosimetry in radiotherapy. J King Saud Univ Sci 2020;32:595-599.
32. Bencheikh M, Didi A, Maghnouj A, *et al*. Empirical Law to Evaluate the Skin Dose with Photon Beam Energy and Irradiation Field Size. Moscow Univ. Phys 2018;73:683-686. Available from: https://doi.org/10.3103/S0027134918060036.
33. Assalmi M, Diaf EY. Dose divergence between Monte Carlo simulation and experimental measurements in the build-up region for a photon beam. Radiat Phys Chem 2021;188:109643.
34. ICRU Report 24: Determination of Absorbed Dose in a Patient Irradiated by Beams of X or Gamma Rays in Radiotherapy Procedures; 1976.
35. Domingo C, *et al*. Neutron spectrometry and determination of neutron ambient dose equivalents in different LINAC radiotherapy rooms. Radiat Meas 2010;45:1391-7.
36. Şakar E, Alim B, Fırat Özpolat O, Ceviz Şakar B, Baltakesmez A, Akbaba U. Asurveying of photon and particle radiation interaction characteristics of some perovskite materials. Radiat Phys Chem 2021;189:109719.
37. Israngkul-Na-Ayuthaya I, Suriyapee S, Pengvanich P. Evaluation of equivalent dose from neutrons and activation products from a 15-MV X-ray LINAC. J Radiat Res 2015;56:919-26.
38. Sahoo GS, Tripathy SP, Molokanov AG, Aleynikov VE, Sharma SD, Bandyopadhyay T. Measurement of LET (linear energy transfer) spectra using CR-39 at different depths of water irradiated by 171 MeV protons: A comparison with Monte Carlo simulation. Nuclear Instruments and Methods in Physics Research Section A, Accelerators, Spectrometers, Detectors and Associated Equipment, 2016. p. 14-19. doi:101016/jnima201602038 .
39. Alpen EL. High Linear Energy Transfer Radiation Effects, in Radiation Biophysics. Radiation Biophysics 1998. p. 365-92. Available from: https://doi.org/10.1016/B978-012053085-4/50016-8.
40. Nenot JC *et al*. The 2007 Recommendations of the International Commission on Radiological Protection. ICRP publication 103. Ann ICRP 2007;37:1-332. doi: 10.1016/j.icrp.2007.10.003.
41. Baiocco G, Barbieri S, Babini G, Morini J, Alloni D, Friedland W, *et al.* The origin of neutron biological effectiveness as a function of energy. Sci Rep 2016;6:34033.
42. Yu O, Chetverikov AA, Bykov AV, Krotov AA, Mistonov MM, Murashev IV, *et al*. Boron-containing plastic composites as neutron shielding material for additive manufacturing processes. Nucl Instrum Methods Phys Res A Accelerators Spectrometers Detectors Assoc Equip 2023;1055:168406.
43. Qi Z, Yang Z, Li J, Guo Y, Yang G, Yu Y, *et al.* The advancement of neutron-shielding materials for the transportation and storage of spent nuclear fuel. Materials (Basel) 2022;15:3255.
44. Airey P, Hinton T, Twining J. The Scientific Basis, Radioactivity in the Environment. Ch. 1, Vol. 18.2012. p. 1-57. Available from: https://doi.org/10.1016/B978-0-08-045016-2.00001-1.
45. Tremsin AS, Shinohara T, Oikawa K, Jiaqi Li, Monteiro PJ. Non-destructive mapping of water distribution through white-beam and energy-resolved neutron imaging. Nucl Instrum Methods Phys Res A Accelerators Spectrometers Detectors Assoc Equip 2019;927:174-83.
46. Bolch WE, Jokisch D, Zankl M, Eckerman KF, Fell T, Manger R, *et al.* ICRP publication 133: The ICRP computational framework for internal dose assessment for reference adults: Specific absorbed fractions. Ann ICRP 2016;45:5-73.
47. El Bakkali J, Doudouh A, El Bardouni T. InterDosi simulations of photon and alpha specific absorbed fractions in zubal voxelized phantom. Appl Radiat Isot 2021;176:109838.
48. El Bakkali J, Doudouh A, El Bardouni T, Ait Sahel O. Monte Carlo calculation of photon specific absorbed fractions in digimouse voxelized phantom using Interdosi code. Radiat Phys Chem 2021;182:109360.
49. Chauvin M, Borys D, Botta F, Bzowski P, Dabin J, Denis-Bacelar AM, *et al.* OpenDose: Open-access resource for nuclear medicine dosimetry. J Nucl Med 2020;61:1514-9.